UTRECHT UNIVERSITY

Tailoring photonic crystal waveguides to create chiral fields

Author:
I.M. Palstra B.Sc.

Supervisors:
N.D. Kosters M.Sc.
Prof. Dr. L. Kuipers

FOM INSTITUTE AMOLF, AMSTERDAM

NANOOPTICS GROUP

July 29, 2016

Abstract

In this work we present a design for a chiral photonic crystal waveguide (PhCW). This chiral PhCW was achieved by breaking all mirror symmetries of a conventional PhCW by adding an SiO_2 substrate and shifting the positions of the air holes along the waveguide. The resulting chiral PhCW exhibits a non-monotonic dispersion of the fundamental mode, shifted field patterns, creation an annihilation of of circular polarization singularities, and a shift in their position. The near-fields above this chiral PhCW have an integrated optical chirality with a value that is 0.16 times that of circularly polarized light. As absorption rates and refractive index in solutions of chiral molecules are chirality-dependent, this chiral PhCW could be used as a first step towards on-chip measurements of chiral purity of solutions of chiral molecules.

Contents

1 Chirality in light and matter 1
1.1 Optical rotation and circular dichroism 1
1.2 The polarization ellipse and polarization singularities 3
1.3 Chirality of electromagnetic fields 4
1.4 Sensing of chiral molecules 6

2 Creating chiral photonic crystal waveguides 8
2.1 Light confinement inside photonic crystal waveguides 8
2.2 Chirality in PhCWs 11
2.3 Symmetry rules of the optical chirality 11
2.4 Maximizing the phase shift induced by chiral interactions 13

3 Simulation results 14
3.1 Design of a chiral PhCW 14
3.2 Band diagrams of achiral and chiral PhCW 14
3.3 Fields profiles of achiral and chiral PhCW 16
3.4 C-points in achiral and chiral PhCWs 17
3.5 Optical chirality in an achiral PhCW 18
3.6 Optical chirality of a chiral PhCW 20
3.7 Discussion 20

4 Outlook 22

5 Conclusions 24

A Computational cells for simulating a PhCW 28

B Optimization of optical chirality 29

C Sample fabrication 30

1 Chirality in light and matter

In nature, chirality is a commonly occurring phenomenon. Any object or system that cannot be superimposed on its mirror image is called chiral. The word “chirality” is analogous with the word “handedness”, and has its origin in the Greek $\chi\varepsilon\iota\rho$, which means hand, as hands are one of the the most well-known examples of chiral objects: Left and right hands are each other’s mirror images, but it is impossible to map all the features onto each other through rotation and translation alone.

Many (bio-)molecules like DNA, sucrose, fructose, and testosterone are chiral. Their mirror images, called enantiomers, often have quite different chemical properties than the original [1]. For example: the left-handed enantiomer of methamphetamine is a nasal decongestant commonly found in vapour inhalers. Its right-handed enantiomer is the street drug known as crystal meth [2, 3]. This is a clear example of how a single structural difference can lead to dramatically different chemical properties.

Similarly to molecules, light can also be chiral. The electric field vector of a beam of circularly polarized light (CPL), for example, will trace out a helix in 3D space. Helices are chiral objects and can either be left- or right handed, corresponding to left- or right handed CPL. Chiral molecules and their enantiomers have differences in the orientation and position of their internal electric and magnetic dipoles. Due to these differences, chiral molecules and their enantiomers will have a different rates of absorption for different handednesses of light [4].

The differences in chemical properties of chiral molecules make quantification of the chiral purity of a compound highly relevant. The chiral purity of a solution of molecules can be experimentally determined by exploiting the chiral interactions between molecules and light [4]. These interactions, and how to use them to do sensitive measurements on chiral molecules, will be the focus of this work.

1.1 Optical rotation and circular dichroism

Absorption of light in a medium is closely related to the refractive index of the medium. In a homogeneous medium, the refractive index of the medium $\tilde{n}$ is a complex quantity $\tilde{n} = n + i\kappa$ with real part n and imaginary part κ. A plane wave travelling with a frequency ω through a homogeneous dielectric medium will have a wave vector that is affected by the refractive index

$$\begin{aligned} \mathbf{E} &= \mathbf{E_0} \exp\big[i(\tilde{n}\mathbf{k}\cdot\mathbf{r} - \omega t)\big] &(1)\\ &= \mathbf{E_0} \exp\big[i(n\mathbf{k}\cdot\mathbf{r} - \omega t)\big] \exp\big[-\kappa\mathbf{k}\cdot\mathbf{r}\big], &(2)\end{aligned}$$

where $\mathbf{E}$ is the complex electric field, $\mathbf{E_0}$ is the field amplitude, and $\mathbf{r}$ and t are the position in space and time, respectively. This electric field has a phase evolution in space governed by n, and a damping rate determined by κ. Thus, the phase is affected by the real part of

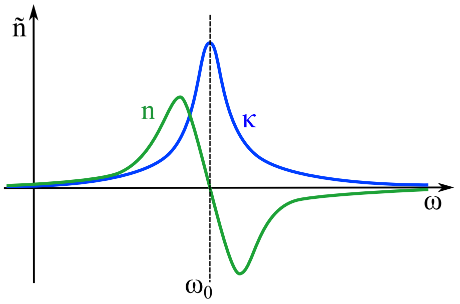

Figure 1: Schematic of the relation between the real and imaginary part of the refractive index, n (in green) en κ (in blue), respectively, as a function of the frequency ω. They are plotted around the resonance frequency ω_0. When ω_0 is approached, the absorption increases and the refractive index of the material changes.

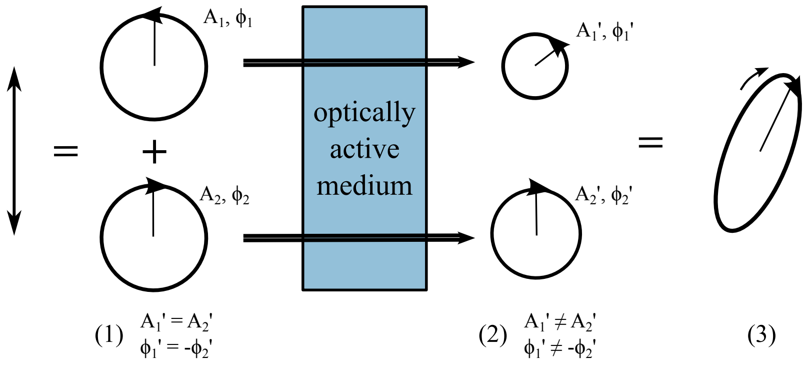

Figure 2: Schematic of optical activity. (1) A beam of linearly polarized light can be described as two overlapping beams of CPL with equal amplitudes $A_1 = A_2$, and opposite phases $\phi_1 = -\phi_2$, which gives them opposite handedness. (2) As the light passes through an optically active medium, both beams have a different absorption (through CD) and a different refractive index (through OR), leading to a difference in amplitude, $A_1 \neq A_2$ and phase $\phi_1 \neq -\phi_2$. (3) This leads to a beam of elliptically polarized light, which is rotated with respect to the optical axis of the original, linear beam.

the refractive index, and the amplitude by the imaginary part. These real and imaginary parts are related through the Kramers-Kronig relations, which state that the absorption of light in a medium and refractive index of that medium are coupled [5, 6, 7]. Figure 1 shows a schematic of the relation between the real and the imaginary part of the refractive index as a function of the frequency for systems with a single resonance at ω_0. As light approaches the resonance frequency, absorption by the medium increases, and the refractive index felt by the light changes with respect to the value away from the resonance [7, 4].

A distinctive property of chiral molecules is that they have different rates of absorption for left and right CPL. This differential absorption is known as circular dichroism (CD). Through the relation between absorption and refractive index, this difference in absorption means that beams of opposite handedness will also experience different refractive indices when propagating through a solution of chiral molecules. This is known as optical rotation (OR), and molecules that exhibit CD and OR are said to be optically active [4, 8].

A schematic of optical activity is shown in Figure 2. (1) A linearly polarized beam of light can be described as two overlapping beams of CPL, with equal amplitudes $A_1 = A_2$ and

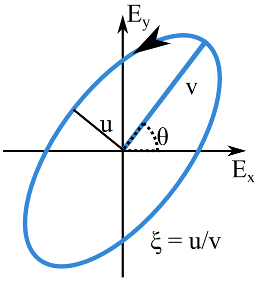

Figure 3: A schematic of the polarization ellipse. The real part of the electric field vector traces out the blue ellipse in time. The angle of polarization is given by θ, the ellipticity of the light is $\xi = u/v$. For linear polarization, $\xi = 0$. For circular polarization, $|u| = |v|$.

opposite phases $\phi_1 = -\phi_2$, so they have opposite handedness. (2) When this beam travels through an optically active medium such as a solution of chiral molecules, circular dichroism will cause one handedness to be absorbed more strongly than the other. This will cause the two beams to obtain different amplitudes, leading to elliptically polarized light. Optical rotation will cause the two beams to acquire a phase shift with respect to each other, which rotates the optical axis of the light. (3) The result is a beam of elliptically polarized light, which is rotated around its centre.

Optical activity changes the polarization state of light. This can be described using the polarization ellipse, which will be discussed below. After this, a more general description of chiral interactions between light and chiral molecules will be discussed.

1.2 The polarization ellipse and polarization singularities

In a general description of light, it is always possible to deconstruct a monochromatic electromagnetic (EM) field in a sum of plane waves. Monochromatic EM fields oscillate with a fixed frequency, causing an electric field vector at a point $\mathbf{r}$ to draw out an ellipse in time [9]. This ellipse is called the polarization ellipse, and it contains information on the polarization state at $\mathbf{r}$. A schematic of the polarization ellipse is shown in Figure 3. The blue ellipse is the path traced out by the electric field vector in time, ξ is the ellipticity, which is defined as the ratio of the semi-minor and semi-major axes u and v. θ is the angle of orientation, and has values that range from $-\frac{1}{2}\pi \leq \theta \leq \frac{1}{2}\pi$, since an ellipse rotated by π is indistinguishable from the original.

Generally, the electric field vector of light will always draw out an ellipse over time, which is a (flattened)helix in 3D space. The handedness of this helix determines the direction in which the ellipse is traced out. Linearly and circularly polarized light are special cases of the polarization, where the ellipse is a line ($\xi = 0$) and a circle ($|u| = |v|$), respectively. Points in space where this occurs, are known as polarization singularities, since the handedness (for linearly polarized light) or the angle of rotation (for CPL) cannot be determined.

There is a special case of polarization singularity, where the light carries orbital angular momentum. In these points, the light is circularly polarized, and the value of θ is singular. These singularities of circular polarization occur in lines in 3D space, or in points when the field is projected on a 2D plane. In these cases, they are referred to as C-lines or C-points, respectively, and are infinitesimal in size [9]. An example of C-point is shown in Figure 4. A path integral over θ around such a singularity will return $\pm\pi$, corresponding to a topological charge of $\pm\frac{1}{2}$. If the polarization ellipse rotates clockwise over a clockwise path around the

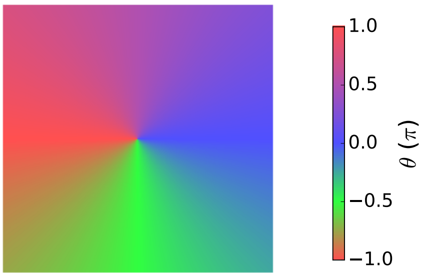

Figure 4: An example of a circular polarization singularity or C-point. The colour scale indicates the value of θ, which is the angle of orientation of the polarization ellipse. In the centre of the figure, in an infinitesimal point, θ is undetermined, so it is a circular polarization singularity or C-point. The topological charge is $+\frac{1}{2}$, as θ rotates by over π around the singularity. The sign is positive because θ increases when a counter-clockwise path is taken around the singularity. This means that the polarization ellipse rotates clockwise on a clockwise path.

singularity, the sign of the topological charge is positive. Else, it is negative. The sign of the topological charge is determined by the type of singularity, and is independent of the handedness of the light in the singularity [10][9].

The polarization ellipse is a useful tool to visualize the polarization state of an EM field. To understand and quantify the influence of chirality in light on chiral molecules, another quantity is needed: the optical chirality. Later on it will be made clear that the polarization state as described by the polarization ellipse and the optical chirality are closely related, but do not provide equivalent information.

1.3 Chirality of electromagnetic fields

The optical chirality is a measure to quantify how chiral an electromagnetic field is. Intuitively, it can be thought of as a measure for how quickly the field lines of an EM field re-orient themselves in space [11]. In CPL, for example, this re-orientation takes place over the distance of a single wavelength.

The optical chirality is given by

$$C(\mathbf{r}) = \frac{\varepsilon_0}{2}\boldsymbol{E}(\mathbf{r}) \cdot \boldsymbol{\nabla} \times \boldsymbol{E}(\mathbf{r}) + \frac{1}{2\mu_0}\boldsymbol{B}(\mathbf{r}) \cdot \boldsymbol{\nabla} \times \boldsymbol{B}(\mathbf{r}), \tag{3}$$

where $E(\mathbf{r})$ and $B(\mathbf{r})$ are the position-dependent electric and magnetic fields, and ε_0 and μ_0 are the vacuum permittivity and permeability, respectively. The optical chirality was introduced by Lipkin in 1964 [12], and it was initially thought to have no physical interpretation. However, it has recently gained attention due to its connection to the asymmetry in excitation of chiral molecules [13]. The asymmetry in the excitation rates of left- and right-handed enantiomers (γ^L, γ^R) is

$$g(\mathbf{r}) \equiv \frac{\gamma^L - \gamma^R}{\frac{1}{2}(\gamma^L + \gamma^R)}, \tag{4}$$

where $g(\mathbf{r})$ is called the dissymmetry factor. It gives the asymmetry of the excitation rates of the enantiomers, if they are exposed to the same EM field. The theoretical limits of this asymmetry are ±2, corresponding to excitation of one enantiomer, but not the other. However, since chirality-independent interactions are generally much stronger than chiral interactions, this limit is not achievable in real molecules [4].

Recently, it was found that the dissymmetry factor scales with the optical chirality:

$$
\begin{aligned}
g(\mathbf{r}) &= \left(-\frac{4G''}{\alpha'' c}\right)\left(\frac{cC(\mathbf{r})}{2\omega U_\mathrm{e}(\mathbf{r})}\right) && (5)\\
&= g_\mathrm{mol}\cdot g_\mathrm{EM}(\mathbf{r}), && (6)
\end{aligned}
$$

where c is the speed of light, ω is the frequency, α'' is the imaginary part of the electric polarizability of the molecules, which is the relative tendency of an electron cloud to be distorted by en external electric field. G'' is the imaginary part of the isotropic mixed electric-magnetic dipole polarizability, which is a measure for the coupling between internal electric and magnetic dipoles, and is responsible for optical activity [4]. For achiral molecules, $G'' = 0$, as achiral molecules are not optically active. $U_\mathrm{e}(\mathbf{r}) = \frac{\varepsilon_0}{4}|E(\mathbf{r})|^2$ is the time-averaged electric energy density of the EM field [13].

A notable property of Equation 5 is that it shows a clean separation of terms that depend only on molecular properties (g_mol), and terms that depend only on the properties of the local EM field (g_EM). The former consists of material-dependent constants, while the latter is a tunable parameter. Together, they determine the asymmetry of the excitation rate of the molecules in question. This implies that by tuning g_EM through the EM fields, one can tune the asymmetric response of chiral molecules.

We define

$$
g_\mathrm{EM} = \frac{cC(\mathbf{r})}{2\omega U_\mathrm{e}(\mathbf{r})} \qquad (7)
$$

form Eqn. 6 as the local optical chirality. It scales with the asymmetric response of a single chiral molecule that is located at $(\mathbf{r})$ with respect to its enantiomer, if it were illuminated by the same field, compared with the asymmetry for CPL. The normalisation with the electric energy density is used because it makes it possible to compare the optical chirality of any field with the optical chirality of CPL. For CPL, the optical chirality is $C = \pm 2U_\mathrm{e}\omega/c$ and $g_\mathrm{EM} = \pm 1$, where the positive signs corresponds to left CPL. For unpolarized or linearly polarized light, $C(\mathbf{r})/U_\mathrm{e}(\mathbf{r}) = 0$ [4].

Recent work has shown that it is possible to construct EM fields where the field lines are more tightly wrapped than that of CPL, and have $g_\mathrm{EM} > \pm 1$, i.e. the value of CPL. EM fields with this property are referred to as superchiral fields. Superchirality generally does not occur in large volumes. Rather, it usually occurs in small hotspots, for instance near a node of the field, or close to plasmonic structures [13, 14, 15, 16]. In CPL, the EM field lines re-orient themselves over a much longer length scale than the size of small molecules, so this “twist” in the field, which is responsible for chiral interactions, is felt only weakly by these molecules. In a superchiral field, the field lines re-orient themselves over a shorter distance, which is closer to the scale of the molecules [11]. Due to this, the asymmetry of the excitation rate of chiral molecules can be greatly enhanced [17, 18, 11, 15].

Currently, the optical chirality C is a frequently-used measure to quantify the chirality of EM fields [19, 15, 20]. Systems with (super-)chiral fields have been used to engineer the direction of the emission of a quantum dot [21], and for the sensitive measurement of chiral molecules [17]. Since superchiral light enhances the chiral response of molecules, nanostructures with an enhanced optical chirality could provide a path towards on-chip measurements of optical rotation. In the following section we present a detection scheme for such a sensor.

1.4 Sensing of chiral molecules

Measurements of optical rotation are typically performed by sending a beam of light with a controlled wavelength and linear polarization though a cuvette, and measuring the amplitude and polarization state of the transmitted light. Since the optical activity scales with the chiral purity, the rotation of a linearly polarized beam can be used to determine the chiral purity of a sample [4]. The same principle can be applied to create an on-chip method to measure optical rotation. This could be used for cheaper measurements in a more highly controlled environment than conventional techniques.

Nanostructures offer a high measure of control over their electric and magnetic near field, and many nanostructures offer the possibility to be fabricated on-chip [22]. In addition to this, their small scale would allow for smaller amounts of solution to be used to perform an accurate measurement than with conventional techniques. This makes them a promising candidate for on-chip sensors of chiral molecules.

Chiral molecules in the near field of a nanostructure will induce a phase shift in a light wave travelling through the structure. In order to measure the induced phase shift, we propose the detection scheme described in Figure 5. The purpose of the proposed sensor is to determine the chiral purity of a solution of molecules through optical rotation. In the setup, a beam of a monochromatic laser is split in two at a beam splitter (BS I). Each beam passes through a nanostructure that is in contact with the molecular solution, which covers both structures. The interactions with the molecules due to the optical chirality of the structures' near field will induce a phase shift ϕ_{C_1,C_2} in each of the beams. Other phase contributions due to interactions with the molecules are collected in $\phi_{\text{rest},1}$ and $\phi_{\text{rest},2}$.

The beams interfere at a second beam splitter (BS II), and pass to two detectors (A and B), in a Mach-Zehnder like interferometer. The total phase of the two beams at the detectors A and B is:

$$\begin{aligned} \phi_{\text{A},1} &= 2\rho + 2\pi + \phi_{C_1} + \phi_{\text{rest},1} + \phi' \qquad & \phi_{\text{B},1} &= \rho + 2\pi + \phi_{C_1} + \phi_{\text{rest},1} + \phi' \\ \phi_{\text{A},2} &= 2\rho + \pi + \phi_{C_2} + \phi_{\text{rest},2} & \phi_{\text{B},2} &= \rho + 2\pi + \phi_{C_2} + \phi_{\text{rest},2}, \end{aligned} \tag{8}$$

where ρ is the phase shift acquired when by a beam when it passes diagonally through a beam splitter, the factors of π result from front reflection off mirrors, and ϕ' is a tunable phase shift. If the nanostructures are identical except for the optical chirality of their near field, $\phi_{\text{rest},1} = \phi_{\text{rest},2}$, and the intensities I on the detectors A and B is given by

$$\begin{aligned} I^A &= I_1 + I_2 + 2\sqrt{I_1 I_2}\cos(\phi_{\text{A},1} - \phi_{\text{A},2}) \\ &= I_1 + I_2 + 2\sqrt{I_1 I_2}\cos(\phi_{C_1} - \phi_{C_2} + \pi + \phi') \end{aligned} \tag{9}$$

$$\begin{aligned} I^B &= I_1 + I_2 + 2\sqrt{I_1 I_2}\cos(\phi_{\text{B},1} - \phi_{\text{B},2}) \\ &= I_1 + I_2 + 2\sqrt{I_1 I_2}\cos(\phi_{C_1} - \phi_{C_2} + \phi'), \end{aligned} \tag{10}$$

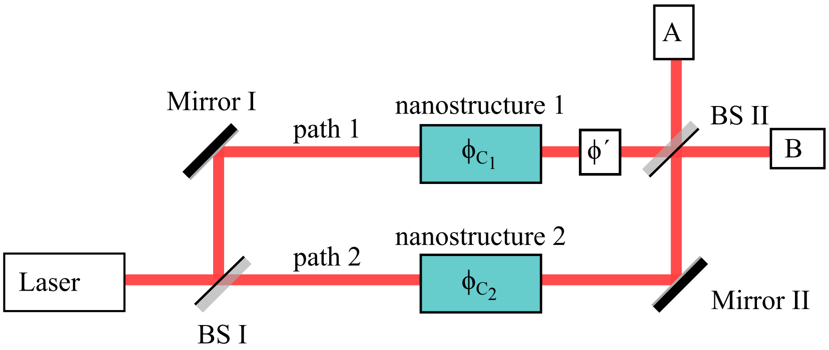

Figure 5: Proposed on-chip detection scheme for chiral molecules. A laser beam is split in two beams at a beam splitter (BS). The light is sent to two nanostructures, which have opposite optical chirality distributions, and are both in contact with a solution of chiral molecules. Optical chirality-dependent interactions with the molecules will induce a phase difference ϕ_{C_1} and ϕ_{C_2} in the two beams, which is measured in the Mach-Zehnder like interferometer; the two beams interfere at a second beam splitter (BS II) and pass to two detectors. In order to determine the sign of the phase shift, a tunable phase shift can be added to the lower branch. From the measured phase difference between ϕ_{C_1} and ϕ_{C_2}, the chiral purity of the solution of molecules can be determined.

where I_1 and I_2 are the intensities of the paths, and ϕ' can be added to determine the sign of the phase shift.

The proposed sensor measures only the difference in phase that is induced by the optical chirality of the structures, and ignores other phase contributions. Ideally, the two nanostructures have opposite optical chirality, so that nanostructure 1 will have an enhanced interaction with one enantiomer of a molecular solution, and nanostructure 2 will have the same enhanced interaction with the other enantiomer. In this case, an equal ratio of both enantiomers in a solution will yield no difference between ϕ_{C_1} and ϕ_{C_2}. This phase difference increases with the chiral purity, and can be used to quantify the chiral purity of a solution of molecules.

As the chiral interactions scale with the optical chirality of the nanostructures, the required nanostructures must have chiral or even superchiral near fields with a preferential handedness to do sensitive measurements. The nanostructures of the proposed sensor must be tailored to optimize their optical chirality, and to achieve exactly opposite g_{EM}

A potential candidate for the nanostructure in the proposed detection scheme are photonic crystal waveguides (PhCW). They have the advantage of having a small scale and being relatively straightforward to make, using commercially available wafers. Recent work has shown that there are lines of circular polarization in the near fields above PhCWs [10], which implies chiral behaviour of the near field. This makes PhCWs a candidate for the proposed sensor.

2 Creating chiral photonic crystal waveguides

2.1 Light confinement inside photonic crystal waveguides

In crystals, the periodic potential of charge density affects the motion of electrons through the material. In photonic crystals, an analogous effect takes place, where a periodic variation in the dielectric function affects the motion of photons in the material. Many different implementations of the concept of photonic crystals exist, such as arrays of dielectric pillars and stacked layers of materials with alternating refractive index. Light that is coupled into a photonic crystal is strongly influenced by the periodicity in the refractive index, especially if the periodicity is on the order of the wavelength of the light. A class of photonic crystals exist called photonic crystal hole slabs. They consist of a thin ($\mathcal{O}(100\text{ nm})$) slab of high-index dielectric, typically silicon, with a periodic array of air holes perforating the slab, as shown in Figure 6a [23]. We shall here consider a silicon slab perforated with a triangular lattice of air holes.

Slabs of dielectric have the ability to confine light. In the ray optics regime, if a beam propagating through a high-dielectric material has a small enough angle of incidence on a dielectric-air interface, it is a solution to Snell's law; the light can couple to free space and will leave the dielectric. If the angle of incidence is larger than the critical angle, the beam will undergo total internal reflection, and light is confined to the dielectric.

In thin films, such as a photonic crystal hole slab, ray optics do not hold, and the conditions for confinement are slightly different. Light in a thin film has a frequency given by $\omega = c|\boldsymbol{k}| = c\sqrt{k_x^2 + k_y^2 + k_z^2}$, where k_x and k_y are parallel to the slab, and k_z is perpendicular to it. The axes are shown in Fig. 7a. In the case of thin films, light with a finite, real k_z can couple to free space and dissipate quickly; they are leaky. These eigenmodes (modes) of the system lie above the light line or light cone, which is given by $\omega \geq c\sqrt{k_x^2 + k_y^2}$. Because light in modes above the light line dissipates, we will consider only modes that lie beneath it. Modes that lie beneath the light line have an imaginary value of k_z; they do not propagate perpendicularly to the slab. Therefore, these modes are confined to the slab, and they decay exponentially away from the it. The part of the light field that "spills" out of the slab is called the evanescent field. The near field of a system is the part of the field where evanescent fields have a significant contribution to the total field.

A photonic crystal hole slab that is suspended in air has mirror symmetry in its $z = 0$ plane, which lies in the slab. This imposes a symmetry on the modes of this system, which can be either even or odd in $z = 0$. In the range of relatively low frequencies that will be considered here, the even modes have an electric field that is mostly polarized in the plane, and resemble transverse electric (TE) modes. The odd modes have an electric field that is mostly polarized out of the plane, and resemble transverse magnetic (TM) modes. Consequently, in the mirror plane that lies in the slab, the electric fields of the even modes are oriented parallel, and the electric fields of the odd modes are oriented perpendicular

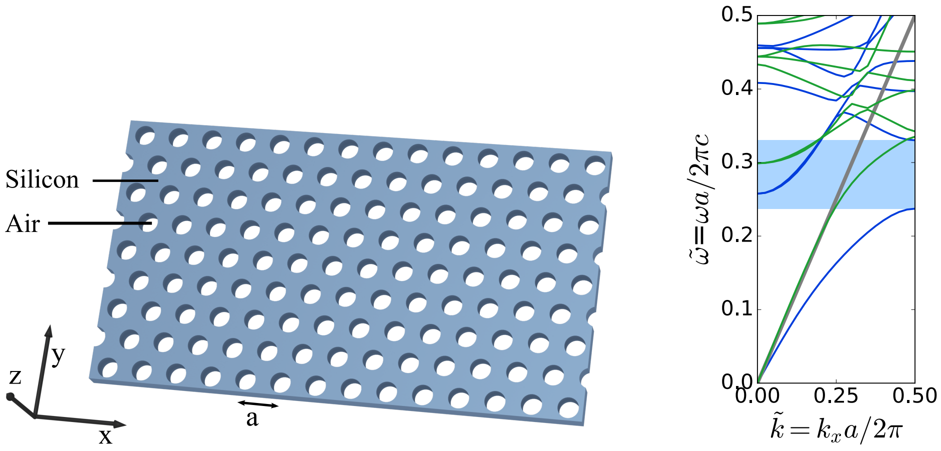

(a) (b)

Figure 6: (a) A photonic crystal hole slab. The blue material represents silicon, which is suspended in air. (b) The band diagram of a hole slab. The even modes are shown in blue, and the odd modes in green. The dispersion for light in vacuum is shown in grey, and the band gap for the even modes is shown in light blue. In this band diagram only values for k in the x-direction are plotted.

to the plane. The mirror symmetry in the slab ensures that the even and odd modes are perpendicular to each other, which ensures that they are decoupled. Due to this decoupling, energy from the even modes cannot dissipate to the odd ones, and vice versa [23].

The presence of the air holes in the slab leads to a different dispersion relation (frequency ω as a function of wave vector k) for propagating light than can be found in bulk materials. The dispersion relation, also called a band diagram, for a photonic crystal slab is shown in Figure 6b. We will only consider non-redundant modes travelling in the positive x-direction in this dispersion relation. In reciprocal space, this corresponds to $0 < k_x a/2\pi < 0.5$, where k_x is the wave vector in the x-direction, and a is the lattice constant of the hole array. The dispersion relations of Fig 6b can be grouped by whether they have even or odd symmetry with respect to the centre plane of the slab at $z = 0$. In the figure, the even modes are shown in blue, whereas the odd modes are shown in green. The dispersion of light in vacuum is shown by the diagonal grey line. This is called the light line.

It is clear from this figure that for odd modes, every frequency has one or more possible values for k_x. Due to this, odd modes can always propagate through the hole array, regardless of their frequency. For even modes, there is a range of frequencies where no values of k_x are possible below the light line. This means that no light of a confined mode within this range can propagate though the hole array; the array acts as a mirror for even modes in this frequency range. This region of forbidden frequencies is called a photonic band gap. It is shown in the light blue band in Fig. 6b. There are even modes in the band gap that lie above the light line. However, these are standing waves in the z-direction. They are not confined to the slab, so bound modes can't couple to them. Therefore, they do not destroy the band gap. The band gap is the basis for creating photonic crystal systems with strong confinement of light and enhanced light-matter interactions, when complemented by the use of certain defects of the crystal. A triangular lattice of air holes is frequently used for such systems because it has a large band gap for even modes [23]. We will use the band gap of the photonic crystal slab to confine light, so we will only consider the even modes of the structure from

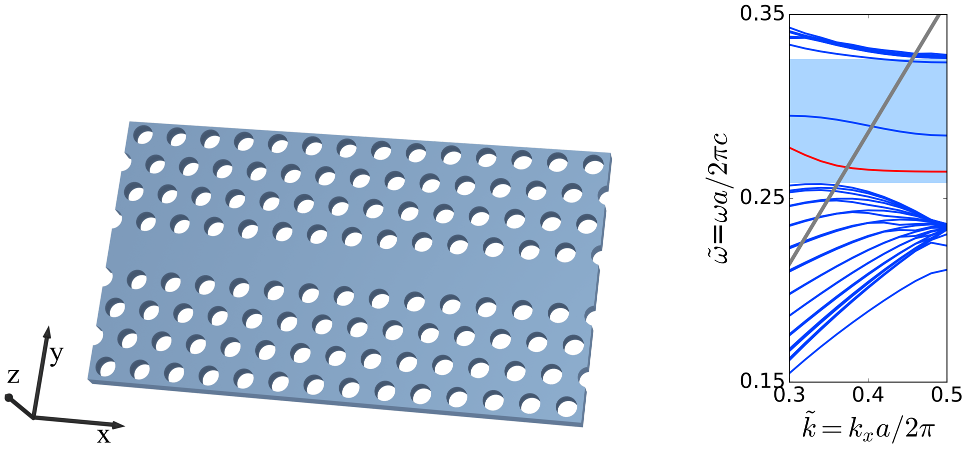

(a) (b)

Figure 7: (a) A photonic crystal waveguide. (b) The band diagram of a PhCW. Here, only the TE modes are shown. The bulk modes are shown in blue, while the fundamental mode of the defect is shown in red.

now on.

A particular defect is created by removing a single row of holes from the hole array of a photonic crystal hole slab to create a waveguide, as shown in Figure 7a. The resulting system is called a photonic crystal waveguide (PhCW). Defects in the bulk of a photonic crystal have their own associated modes, called defect modes. The mode that will be considered in this work is the lowest-frequency defect mode of the row of missing holes. Recently, PhCW systems have grown into an avidly studied field due to their ability to confine light inside the row of missing holes [23].

In the band diagram of the PhCW, the band gap for even modes is the same as that of a photonic crystal hole slab, and is highlighted in blue in Figure 7b. In this figure, far more modes outside the band gap are visible. The smallest possible unit cell of the photonic crystal holes slab contained a single air hole. For the PhCW, the unit cell contains many more rows of holes in the y-direction of Fig. 7a. The extra modes are a consequence of the resulting periodicity in the y-direction, and will be referred to as the bulk of the modes. In addition to this bulk, there is an appearance of two modes that lie inside the band gap. These are eigenmodes of the defect. For the purpose of the biosensor, we will consider only the lowest-order mode of the defect, shown in red in Fig. 7b.

In PhCWs, there are two mechanisms that confine the light of the defect modes in the line defect, which are caused by the hole array. The first is called index guiding. PhCWs mostly operate in the infrared regime (1.4-1.6 nm), where silicon is transparent [24, 25, 26]. At these wavelengths, the hole array is a subwavelength feature, so the light experiences an effective refractive index, which is a spatial average of the physical refractive indices. The presence of the air holes lowers the effective refractive index of the hole array with respect to that of the missing hole row. This confines the mode to the row of missing holes through the same mechanism of generalized total internal reflection that was discussed above.

The second mechanism of light confinement to the missing hole row is that of the photonic band gap. Modes that have a frequency in the band gap, can't propagate into the bulk of the crystal. This means that they are confined to the defect, and these defect modes decay exponentially into the bulk crystal. Through index guiding and defect confinement, the fundamental mode, which has light in the row of missing holes of a PhCW, is confined to this line, and the line defect acts as a waveguide. [27, 23]. Due to this guiding of the mode, real values are only permitted for $k_{||} = k_x$, which is why we consider only these values of $\mathbf{k}$.

In addition to these properties of confinement, PhCWs can be tuned to slow down the light travelling through the waveguide [28]. Linear light-matter interactions such as electro-optic interaction are know to scale linearly with a measure for the "slowness" of light in a system, known as the slowdown factor [28, 29]. The slowdown factor is defined as the ratio of the phase velocity over the group velocity: $S = v_\phi/v_g$. The group velocity is given by the slope of the dispersion: $v_g = d\omega/dk$. This means that a flat band in the dispersion relation corresponds to slow light and a high slowdown factor. By tuning PhCWs, slowdown factors of 60 or more can be achieved, greatly enhancing light-matter interactions [30]. Enhancement of light-matter interactions is a desirable property for the biosensor nanostructure discussed in Section 1.4.

2.2 Chirality in PhCWs

The circular polarization singularities above PhCWs imply chiral behaviour of the near fields. In every period in the x-direction of the waveguide, there are two C-points on either side of the waveguide [10]. This gives a strong indication for the presence of chiral fields above PhCWs, which are necessary for the application of creating the biosensor proposed in Section 1.4, as fields with a nonzero optical chirality have a preferential interaction with enantiomers of chiral molecules.

In an EM field, the local intensity may vary, which can make the normalization of C by the local electric energy density, as was done for g_{EM}, problematic. The absolute excitation rates of molecules scale, to first order, with the intensity. Therefore, to determine the total response of an ensemble of molecules in a spatially varying EM field, we must consider C without the local normalization. Therefore, we define this preferential handedness as the total optical chirality

$$g_{\text{tot}} = \frac{2c}{\varepsilon_0 \omega} \frac{\int_{air} C(\mathbf{r}) dV}{\int_{air} |E(\mathbf{r})|^2 dV}, \tag{11}$$

where both the integrals are taken over free space; the air around the slab and inside the air holes. This is the space that would be occupied by a molecular solution in an optical rotation measurement. The total optical chirality gives the optical chirality of the entire near field above the structure, normalized by the electric energy density. For CPL, $g_{\text{tot}} = \pm 1$. For the proposed biosensor, we need a PhCW with a nonzero g_{tot}, and another PhCW with the opposite g_{tot}. In order to find a PhCW with nonzero g_{tot}, the symmetry properties of PhCWs must be considered.

2.3 Symmetry rules of the optical chirality

To understand the role of symmetries in optical chirality it is useful to consider an alternative form of C. Through the Maxwell equations and the identity: $\partial_t \mathbf{B} \cdot \mathbf{E} - \partial_t \mathbf{E} \cdot \mathbf{B} = \omega \operatorname{Im}(\mathbf{E}^* \cdot \mathbf{B})$, we can transform C from Eqn. 3:

$$C = -\tfrac{\epsilon_0}{2} \omega \operatorname{Im}(\mathbf{E}^* \cdot \mathbf{B}). \tag{12}$$

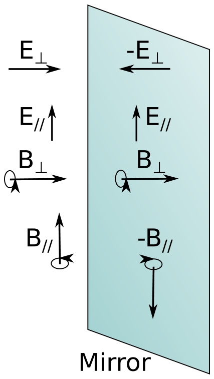

Figure 8: Mirror-symmetry properties of E and B fields. Under mirror symmetry, $E_\perp \to -E_\perp$, $E_{||} \to E_{||}$, $B_\perp \to B_\perp$, $B_{||} \to -B_{||}$.

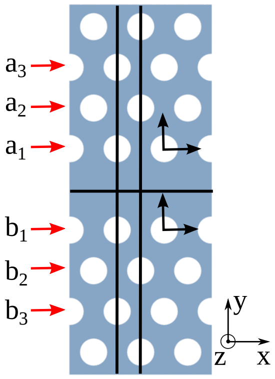

Figure 9: The mirror planes of a PhCW, here shown in black lines. These mirror planes need to be broken in order to achieve nonzero total optical chirality. This can be done by shifting the a_1 and b_1 rows in the x and y directions.

In a system with a mirror symmetry, the EM fields are bound to this symmetry, as is shown in Fig. 8. An electric field component that is perpendicular to a mirror plane will be inverted in the mirror image. A parallel E-field component will have the same sign on either side of the mirror symmetry. For the magnetic field components, these symmetry rules are reversed. A perpendicular B-field component will keep the same sign, and a parallel component will be flipped. The inner product of Equation 12 can be decomposed into components: $\mathbf{E}^* \cdot \mathbf{B} = \mathbf{E}^*_{||} \cdot \mathbf{B}_{||} + \mathbf{E}^*_{\perp} \cdot \mathbf{B}_{\perp}$, where $||$ stands for components parallel to a mirror plane of the system, and $\perp$ for those perpendicular to it. Under mirror symmetry, both components will pick up a sign, so C is anti-symmetric under every mirror plane. To make a system that has eigenmodes with a nonzero value of g_{tot}, every mirror plane in the PhCW system must be broken.

In a regular PhCW, there are four symmetry planes per unit cell. One of the symmetries is the $z = 0$ symmetry, which lies in the plane of the PhCW. A straightforward way to break this symmetry is to place a glass substrate beneath the PhCW, using the refractive index difference between the glass below and the air above the PhCW to break the top-down symmetry.

The three symmetry planes that remain are shown in the black lines in Figure 9. These can be broken by changing the position of the rows of holes along the waveguide. For clarity, the PhCW air holes were labelled a_1, a_2, and a_2 above the waveguide, and b_1, b_2, and b_3 below it, where the a_1 and b_1 holes are closest to the waveguide. Since the EM field is mostly localized in the waveguide due to the confinement described above, the rows that will have the largest impact on the optical chirality when shifted are the two rows adjacent to the waveguide, i.e. the a_1 and b_1 rows. It will be these rows of holes that will be shifted. Any shift of these rows of holes along the waveguide (except a half-period shift in the x-direction) will break the symmetries in the yz-plane, and shifting the a_1 and b_1 rows over a different distance will also break the symmetry in the xz-plane.

The glass substrate beneath the PhCW has a consequence for the system. Since the refractive index of glass is higher than that of air, the speed of light is reduced and light line in the band diagram changes $\omega = ck \to \omega = ck/n_{\text{glass}}$. The light line for a PhCW with a glass substrate is lower than it was before the addition of a substrate. Since all modes above the light line are leaky, it is important that the wave vector chosen for this system is sufficiently high, in order to be far away from the light line to minimize losses.

In addition to this, a flat band of the fundamental mode is also desirable, as these areas have a small group velocity and therefore a high slowdown factor. In an achiral PhCW, the fundamental mode becomes more flat towards at high values of k, near the edge of the first Brillouin zone. Because of this, we choose a wave vector of $k = 0.49a/2\pi$, where a is the lattice constant of the hole array.

In the above sections it was shown that to achieve a nonzero g_{tot}, the mirror symmetries of the system need to be broken. From the asymmetrical behaviour of the optical chirality, it is also clear how to create two PhCWs with opposite g_{tot}. Since the optical chirality is asymmetric under mirror symmetry, so is g_{tot}. If a single PhCW is designed with optimized g_{tot}, its mirror image will have opposite g_{tot}. These two mirrored PhCWs can form the two nanostructures required for the proposed biosensor.

2.4 Maximizing the phase shift induced by chiral interactions

In the proposed biosensor, measurement of the phase difference between the two paths will give information on the chiral purity of the sample. Since optical activity effects are typically weak [4], it is important to maximize the phase shift induced by the molecules. There are some quantities that can be expected to scale, to first order, with the phase shift, such as the total optical chirality of the system, and the concentration and rotating power of the molecules. This gives the following scaling relation for the phase shift from a single chiral PhCW:

$$\Delta\phi \propto [\alpha]_{\lambda}^{20} \cdot \rho \cdot g_{\mathrm{tot}} \cdot L \cdot S. \tag{13}$$

Here, $[\alpha]_{\lambda}^{20}$ is the rotatory power of the molecules at 20°C at a wavelength λ. ρ is the concentration of the molecules, g_{tot} is the total optical chirality of the near field, L is the length of the waveguide, and S is the slowdown factor.

The typical operating wavelength of PhCWs is in the 1.4-1.6 μm range, although molecular resonances are typically in the visible or ultraviolet regime [4]. The Drude equation gives an estimate of how the rotatory power of molecules changes as the excitation wavelength is brought further from their resonance:

$$[\alpha]_{\lambda}^{20} = \sum_{j} \frac{A_j}{\lambda^2 - \lambda_j^2}, \tag{14}$$

where the sum is over all the resonances of the molecule j, A_j is a constant appropriate to the absorption at λ_j, and λ is the wavelength used to excite the atoms. The further λ is away from resonance, the smaller the chiral interaction [4].

To achieve a maximum phase shift, the PhCW must be as long as possible while still keeping a measurable transmission. The PhCW must be optimized to operate at a wavelength that is as close as possible to the resonance frequency of the chiral molecules, and to have a high slowdown factor and a high total optical chirality. We will focus on optimizing the PhCW to achieve a high optical chirality.

3 Simulation results

3.1 Design of a chiral PhCW

For the design of the photonic crystal waveguide, the silicon slab was chosen to be 220 nm thick. The lattice constant a of the air holes is 420 nm, in a triangular lattice. The air holes are cylindrical, and have a radius of 120 nm. These parameters of the PhCW yield a large band gap, which is desirable when confining light [23]. A row of missing holes forms the waveguide, as discussed above.

To determine the complex components of the electromagnetic near fields of PhCWs, the eigenfrequencies and field components of the PhCW defect mode were numerically calculated using the MIT Photonic Bands (MPB) package [31]. In these simulations, a computational cell contains a single period a in the x-direction (along the waveguide), 22 rows of holes in the y-direction, and the height of the cell in the z-direction is 4 times the thickness of the silicon slab; the (x, y, z) dimensions of the cell are (a, $11\sqrt{3}a$, 880 nm), where a=420 nm. A full description of the computational cells can be found in Appendix A.

MPB assumes periodic boundary conditions (PBC) in all directions, which is undesirable in the y and z-directions. To circumvent this problem, the unit cell is taken to be sufficiently large in the y and z directions. Since the field decays exponentially away from the slab and the defect, the effect of PBC will be small far away from these areas.

To determine the best position of the air holes to achieve the highest total optical chirality g_{tot}, a four-dimensional parameter sweep was done for the positions of the rows of holes on either side of the waveguide. For each position of the holes, the EM field components were computed. The total optical chirality was calculated for every point in this parameter space, and the one with the highest value was selected. The values of the parameter sweep can be found in Appendix B. The final design of the waveguide is shown in Fig 10a. For comparison, a top view of the achiral and chiral PhCW are shown in Figs. 10b and 10c. They contain two unit cells of the PhCW side by side, and show three rows of holes on either side of the waveguide. In this chiral PhCW, the first row of holes above the waveguide, the a_1 row, was shifted in the x and y directions by $(0.29, 0.20)a$, respectively. The first row of hole below the waveguide, the b_1 row, was shifted only in the x-direction by $+0.60a$. For this optimized structure, we will examine the calculated modes in more detail.

3.2 Band diagrams of achiral and chiral PhCW

The band diagrams of the achiral and chiral PhCW are shown in Figures 11a and 11e, respectively. The band structure of the achiral PhCW are known from literature [23], but the dispersion of the chiral PhCW is somewhat different. To investigate the difference between the achiral and chiral PhCW band diagrams, several band diagrams were calculated, for hole shifts in between those of the chiral and achiral PhCW, with equidistant fractions ζ of the total shift, where ζ has values from zero to one: ζ = (0, 0.25, 0.5, 0.75, 1). For example, at $\zeta = 0.5$, the holes are halfway in between the positions of the achiral and chiral PhCW.

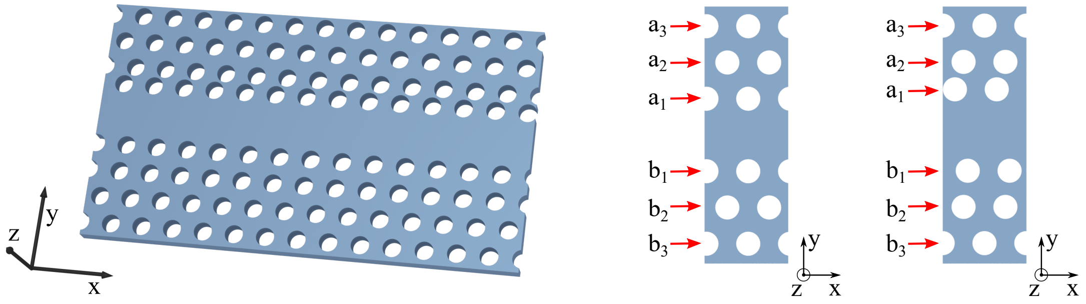

(a) (b) (c)

Figure 10: (a) Design for a chiral photonic crystal waveguide. There is a glass substrate beneath the 220 nm silicon slab, which is not shown here. (b) An achiral PhCW and (c) a chiral PhCW. The range between the a_3 to the b_3 rows are shown, with two unit cells side by side.

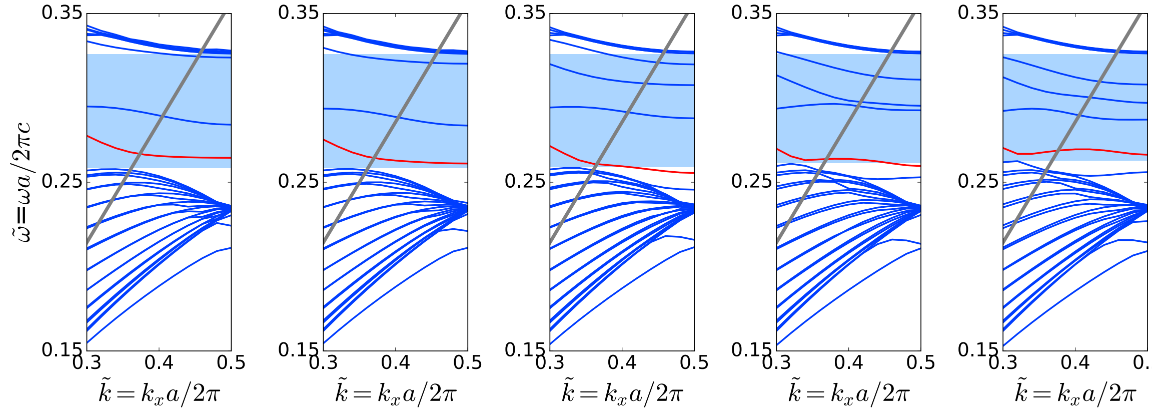

(a) ζ=0, achiral (b) ζ=0.25 (c) ζ=0.5 (d) ζ=0.75 (e) ζ=1, chiral

Figure 11: Band diagrams of a PhCW for different positions of the two rows of holes adjacent to the waveguide. Here, $\tilde{k}$ is the dimensionless wave vector $\tilde{k} = k_x a/2\pi$ and $\tilde{\omega}$ is the dimensionless frequency $\tilde{\omega} = \omega a/2\pi c$. The band gap is shown in light blue. The blue lines outside the band gap indicate the bulk of the modes. The lines inside the band gap are the defect modes, of which the red line is the fundamental mode. The silicon light line is given by the grey, diagonal line. As ζ increases, the shape of the fundamental mode changes, and it leaves the band gap between $0.5 \geq \zeta \geq 0.75$.

Although every waveguide with $\zeta \neq 0$ is chiral, only the PhCW with $\zeta \neq 1$ will be referred to as the chiral PhCW. The band diagrams for $0 < \zeta < 1$ are shown in Figures 11b-11d.

The defect mode of the achiral waveguide (the red band in Fig. 11a) starts as a monotonic, decreasing function, but as the holes are shifted to the position of the chiral waveguide, the mode becomes non-monotonic, exhibiting a bump near the silica light line, after which it decreases, and becomes flat near the edge of the Brillouin zone. Remarkably, the fundamental mode is partially outside the band gap for $\zeta = 0.5$ and $\zeta = 0.75$.

As ζ is increased, two higher-order defect modes appear inside the band gap. They to have dropped down out of the bulk of modes above the band gap. In addition, another band has appeared below the fundamental mode, which is only above the bulk for $\tilde{k} > 0.42$.

3.3 Fields profiles of achiral and chiral PhCW

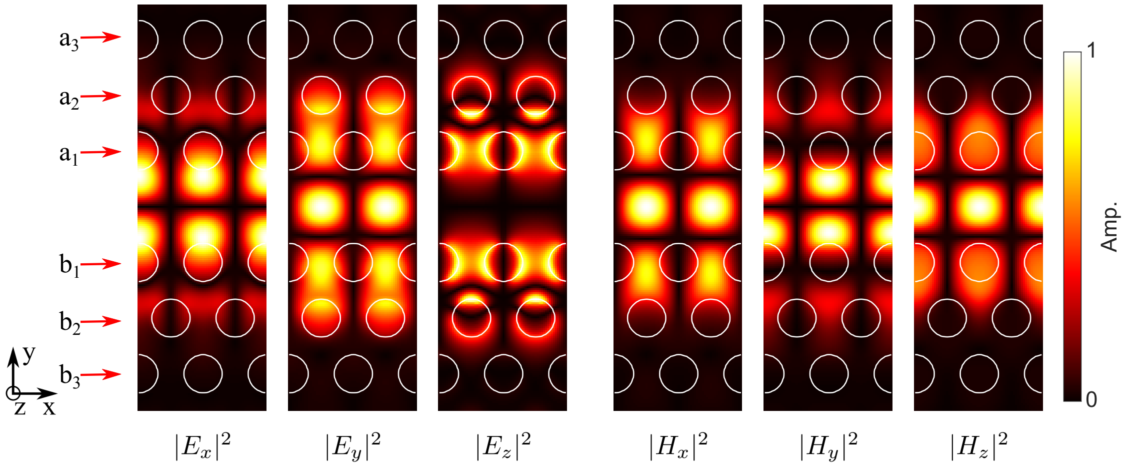

Figure 12: Simulated field intensities of the electric field components of the electric and magnetic field for the chiral PhCW, 20 nm above the surface of the slab. In every frame, the range of the a_3 to the b_3 rows is shown, with two unit cells side by side, and the intensities are all normalized to one.

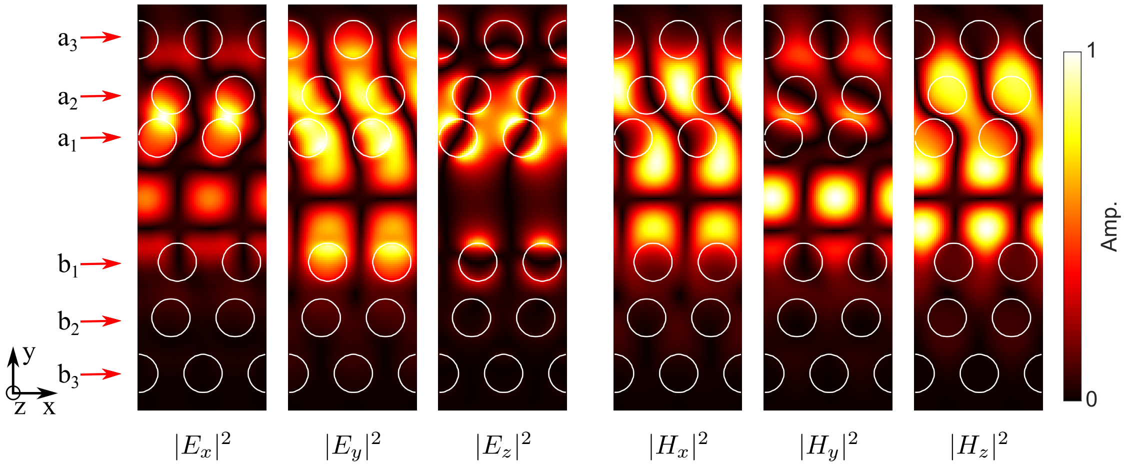

Figure 13: Simulated field intensities of the electric field components of the electric and magnetic field for the chiral PhCW, 20 nm above the surface of the slab. In every frame, the range of the a_3 to the b_3 rows is shown, with two unit cells side by side, and the intensities are all normalized to one.

Measurements of the near fields of PhCWs typically occur several tens to a few hundreds of nm above the surface of the silicon [32]. We will consider the field profiles of our PhCWs 20 nm above the surface of the silicon. The field intensities of the chiral and achiral PhCWs, as found in simulations, can be seen in Figures 12 and 13. The free space wavelength of the fundamental mode was found to be 1570 nm at $k_x = 0.49$. In these figures the range of the a_3 to the b_3 rows is shown, with two unit cells side by side. As the relative field intensities are not important here, all field components are normalized to 1.

The fields of the achiral PhCW are known from literature. In this system, the symmetry

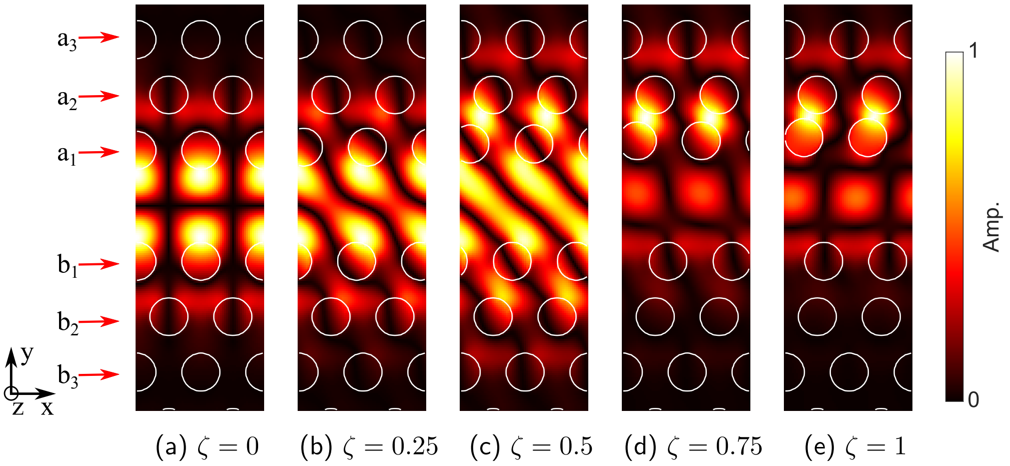

(a) $\zeta = 0$ (b) $\zeta = 0.25$ (c) $\zeta = 0.5$ (d) $\zeta = 0.75$ (e) $\zeta = 1$

Figure 14: Simulated profile of $|E_x|^2$ in the transition from an achiral to a chiral PhCW. Every frame is taken for a different position of the holes, progressing from the achiral PhCW (left), to the chiral PhCW (right)

planes of the PhCW are imposed on the intensity profiles, which are symmetrical in these planes [23]. In the chiral PhCW, these symmetry planes no longer exist, which is reflected in the intensity profiles; these do not exhibit any symmetries. In addition, the regions of high intensity have shifted to the region of the a_1 to a_3 holes, whereas the relative intensity in the b_1 to b_3 region has decreased. In contrast, for the achiral PhCW, the fields were mostly confined to the region between the a_2 and b_2 holes. As discussed above, the light is confined to the missing hole row by index guiding and the guiding due to the band gap. In the achiral PhCW, the defect was only a single row wide. When the holes were shifted, the defect became three rows wide. This leads to a wider distribution of the field in the y-direction.

There are several similarities between the field profiles of the chiral and achiral PhCW. However, when ζ is varied in steps, it becomes clear that the field profiles exhibit a complex behaviour. The intensity profile of E_x, as the holes are shifted in steps, is shown in Figure 14. The same values of ζ were taken as in Figure 11. In Fig. 14, lobes of the field connect diagonally with the smallest shift in hole position from the achiral PhCW. The reason for this is not easily explained, and requires further investigation to understand.

3.4 C-points in achiral and chiral PhCWs

With the calculated field components, the polarization singularities can be found. In thin films, the polarization ellipse is often considered parallel to this film [24]. This is an approximation that is only completely true in the centre plane of the film. Away from this plane, a small out-of-plane component of the electric field slightly tilts the polarization ellipse. Here we will consider the polarization ellipse parallel to the slab of the PhCW.

The C-points were found by plotting maps of θ, shown in Figure 15, for a chiral and an achiral PhCW, and for three equidistant steps in between, with the same values of ζ as in Figures 11 and 14. The C-points were found by eye at the points where lines of constant θ intersect. In each figure, the range between the a_3 to the b_3 rows is shown, with two unit cells side by side, and the C-points are indicated on the left of the two by white dots. In both the chiral and the achiral PhCW, there are points around which θ changes by $\pm 2\pi$ in stead

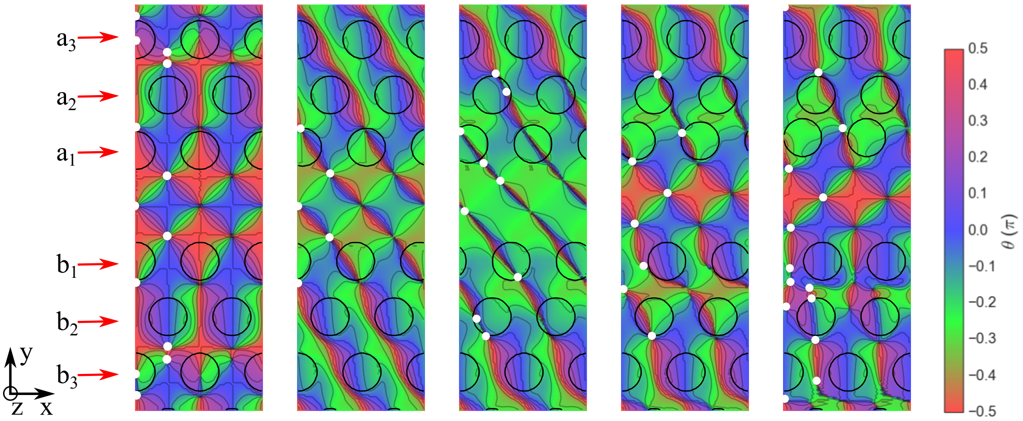

(a) $\zeta = 0$ (b) $\zeta = 0.25$ (c) $\zeta = 0.5$ (d) $\zeta = 0.75$ (e) $\zeta = 1$

Figure 15: Location of polarization singularities in a chiral and achiral PhCW. The C-points are indicated with white dots on the left of the two unit cells shown. As ζ increases, the position of the C-points changes, and they are created and annihilated.

of $\pm\pi$, within the resolution of the calculations. At this resolution, this means that there must be two C-points within 13 nm of each other, illustrating the infinitesimal size of these singularities.

When the a_1 and b_1 rows of holes are shifted with respect to their initial positions, the positions of the C-points in the unit cell changes. In addition to this, the number of C-points is not constant. It is possible for C-points to be created and annihilated with each other, if they have the correct geometry and topological charge [9, 32]. It appears that C-points of the PhCW are created and annihilated as the holes are shifted. When $\zeta = 0.25$, there are eight less C-points in the unit cell than in the achiral PhCW. The C-points near the a_2 and a_3 rows have annihilated with each other, as have the C-points near the b_2 and b_3 rows. At $\zeta = 0.5$, four new singularities have appeared: one pair is close to the a_2 holes, and the other inside the b_2 holes. When ζ goes from 0.75 to 1, several more C-points appear in the region between the b_1 and b_3 rows.

The shift of C-points in the plane above the chiral PhCW and the altered intensity profiles give an indication that the near field of the chiral PhCW is itself chiral. However, for the desired biosensor, the C-points do not give enough information to determine the asymmetric response of chiral molecules. For this, the optical chirality of the chiral PhCW must be considered.

3.5 Optical chirality in an achiral PhCW

Using the six field components, the optical chirality C and the local optical chirality g_{EM} are calculated, using Eqns. 7 and 12. The results for the local optical chirality of the achiral PhCW are shown in Fig. 16a. The colour scale is taken to be linear for a range around zero, and symmetrically logarithmic outside that range. The linear range is $-0.03 < g_{\mathrm{EM}} < 0.03$ and is indicated in the colour scale. In this figure, the positive(negative) values correspond to left(right)-handed optical chirality, and the C-points are indicated with black dots.

Next to the a_1 and b_1 holes, on the side that is farthest from the waveguide, hotspots of superchiral light are visible, in pairs of opposite handedness. Each hotspot extends, with decreasing g_{EM}, to the edge of the line defect. The highest value for the optical chirality

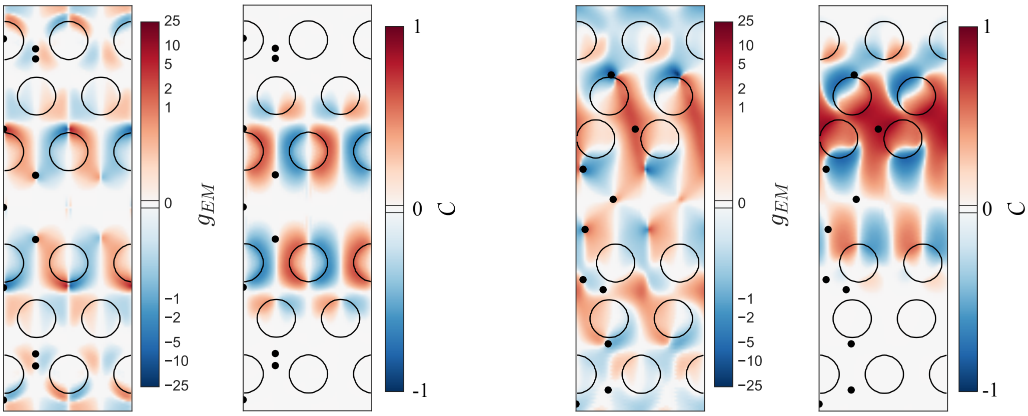

(a) (b) (c) (d)

Figure 16: g_{EM} and C of an achiral (a,b) and a chiral (c,d) PhCW. Positive(negative) values correspond to left(right)-handed optical chirality. The colour scale is linear in the range indicated by the black lines, and symmetrically logarithmic outside it. The range between the a_3 to the b_3 rows is shown, with two unit cells side by side. C-points are indicated by the black dots on the left unit cell.

in the fields at 20 nm above the PhCW is $g_{\mathrm{EM}} = 10$, which is 10 times higher than CPL. The highest value of the local optical chirality in the air above the PhCW can be found at the silicon-air interface. Here, every superchiral hotspot next to the a_1 holes has a value of $g_{\mathrm{EM}} = \pm 24$.

Whereas the local optical chirality g_{EM} is normalized by the local electric energy density, the optical chirality C, as given in Eqn. 3, is unnormalized. Therefore, it takes into account that the contribution of a volume at $\mathbf{r}$, to the total chiral response of an ensemble of chiral molecules, scales with the intensity of the EM field at $\mathbf{r}$. So if we want to visualize the differential rate of absorption, we must consider a map of C, shown in Figure 16b. This figure also uses a symmetrical logarithmic colour scale. As C scales with the intensity, is has been normalized to ±1, and the linear scale is taken in the range $-10^{-2} < C < 10^{-2}$ The relative contribution of the area's close to the waveguide has increased, due to the high relative intensity.

A notable feature in the field maps of g_{EM} and C of the achiral PhCW are the planes of anti-symmetry in every mirror plane of the system, which were predicted in Section 2.3. Every field component with right-handed optical chirality is paired with a component with left-handed optical chirality on the other side of a mirror plane. These parts exactly cancel each other out, so that the total optical chirality of the system, g_{tot}, is zero. This confirms the prediction that an achiral PhCW is not suitable for the detection of chiral molecules, even though strong superchiral hotspots are present in the near fields.

Initially, the C-points in the near fields of Figure 15 seemed like a promising lead to the chiral behaviour of the near fields of PhCWs, since the light at the C-points is circularly polarized. However, the optical chirality map of the achiral PhCW show that the C-points are positioned on the symmetry planes of the PhCW. So, remarkably, these singularities with circular polarization apparently have zero optical chirality. The solution to this paradox lies in the definition of chiral objects and the behaviour of evanescent fields.

In a true evanescent field, the out-of-plane component (z) of the EM fields is purely imaginary, so there is no phase evolution in the z direction. A polarization ellipse perpendicular to this evanescent component will not draw out a helix in the z-direction, but a (flattened) cylinder, which is not a chiral object. This means that elliptical or even circular polarization in an evanescent field in no guarantee of optical chirality.

3.6 Optical chirality of a chiral PhCW

In the process of shifting the holes to obtain a chiral PhCW, the field map of the local optical chirality has changed, as shown in Figure 16c. The symmetrical pairs of (super)chiral hotspots have disappeared. Instead, strong right-handed (negative sign) superchiral hotspots appear below the a_1 holes, and another one above the a_2 holes. A strong hotspot with left handedness connects the two. At 20 nm above the slab, the strongest values of right- and left-handed optical chirality are $g_{\mathrm{EM}} = -24$ and $+19$, and are positioned just above the a_2 holes and below the a_1 holes, respectively. The highest value for the local optical chirality of the chiral PhCW in air has a value of $g_{\mathrm{EM}} = -62$. It is directly above the point with $g_{\mathrm{EM}}{=}{-24}$, at 200 nm above the silicon. Compared to the achiral PhCW, the superchiral hotspots of the chiral PhCW in the region of a_1-a_3 have grown stronger, whereas the hotspots on the b_1-b_3 half are weaker with respect to the achiral PhCW.

In the achiral PhCW, the C-points occurred on the nodes of the local optical chirality field. In the chiral PhCW, they are not exactly in the nodes any more, but off to one side of it. All of them are close to a node, except one, which is in the centre of a strong superchiral hotspot to the left of the a_1 holes. This is an example of a C-point with a high optical chirality The rest of the C-points have a relatively low g_{EM}.

The total optical chirality of the chiral PhCW has a value of $g_{tot} = 0.16$, so over the range of this photonic crystal, an ensemble of molecules would have an excitation asymmetry that is 0.16 times the value if they were illuminated with a beam of left CPL with the same intensity. This shows that it is possible to create a PhCW of which the near-fields have a nonzero optical chirality.

3.7 Discussion

In the numerical simulations presented above, it was assumed for simplicity that, although the substrate broke the $z = 0$ symmetry, the modes are still perfectly even and odd in the $z = 0$ plane. Due to the small difference in refractive index between the air and glass compared to that of silicon, this is a credible assumption. If the proposed biosensor were realized, the surface of the PhCW used would be covered in an aqueous solution. Since the refractive index of water is close to that of glass ($\varepsilon_{H_2O} = 1.7$), the $z = 0$ symmetry would increase, and the assumption would improve.

The chiral PhCW presented above could form the basis of on-chip biosensor measurements. A PhCW has the benefit of slowing down light passing through it, which could enhance light-matter interactions by an order of magnitude [33, 34]. However, the optical chirality of the near fields of the chiral PhCW are an order of magnitude smaller than that of CPL. In addition to this, silicon PhCWs are typically operated in the infrared ($\lambda \sim 1.5\mu$m), where silicon is transparent [32, 35, 23]. The resonance of chiral molecules is usually in the visible or in the near-infrared. Through the Drude equation, shown in Eqn. 14, the phase shift will shrink by an order of magnitude due to this mismatch in frequencies.

Due to the problems associated with the current chiral PhCW, the phase shift of the light in a chiral PhCW will be smaller than that in conventional OR measurements, potentially making it unmeasurably small. Scaling down the PhCW and using a material that is transparent for visible light would allow one to approach the resonance frequency further. Tuning the PhCW to have a higher slowdown factor and a higher optical chirality would also increase the sensitivity of the sensor.

The goal of finding a structure with chiral near fields was to induce a phase difference between two paths when the structure is brought into contact with a solution of chiral molecules. For this, a PhCW was needed of which the total optical chirality is nonzero. The numerical results show that such a chiral PhCW is theoretically possible, but they are yet to be confirmed experimentally. It has been demonstrated experimentally that the field components of a PhCW can be determined using a phase-sensitive near-field scanning optical microscope (NSOM) [25, 32]. The same method could be used to find the near field components of the chiral PhCW presented here.

4 Outlook

In order to approach a chiral PhCW that is suitable for the proposed biosensor, it is necessary to increase the total optical chirality g_{tot} of the near fields. Since sweeping the entire 4D parameter space of the positions of the air holes is computationally expensive, a global optimization technique is preferable to optimize the positions of the a_1 and b_1 rows of holes. In order to achieve higher values of g_{tot}, other parameters, e.g. the radii of the a_1 and b_1 holes could be varied.

The simulation predictions in this thesis have not yet been experimentally confirmed. We propose near field optical scanning microscope (NSOM) measurements in order to experimentally determine the field components of the presented design of a chiral PhCW. Recent work has shown that, using a polarization-sensitive NSOM, the different field components of a near field can be separated to come to a full vectorial mapping of the EM fields [25, 32]. We propose the following sample design suitable for such an NSOM measurement.

Although we do not present measurement results here, the three types listed below were fabricated on a silicon wafer. More information on the fabrication process can be found in Appendix C.

In order to excite the fundamental mode of the PhCW, light is coupled into the silicon film using end fire coupling. In order to minimize noise by light scattering from the edge of the sample, the PhCWs are placed at least 1 mm away from the edge of the substrate. A 1570 nm laser spot is focused on the end of a rectangular waveguide is 3 μm wide, 220 nm high and 1.3 mm long, and is connected to the PhCW.

In order to be able to separate the x and y components of the fields, the NSOM needs to be calibrated with the fields of an achiral PhCW [25]. To minimize misalignment that could occur when moving the probe towards the achiral PhCW, the two types of PhCWs must be paired close to each other on the sample. We propose three types of PhCW that can be etched on the sample. These three types are shown in Figures 17a, 17b and 17c.

Type 1 consists of two PhCWs, an achiral PhCW (above) and a chiral PhCW (below), connected by a Y-junction, as shown in Figure 17a. This junction is connected to a single incoupling rectangular waveguide. The entrance of the Y-junction is 0.5 μm, and the end of the rectangular waveguide tapers from 3 μm to this width over the last 70 μm before connecting to the Y-junction. The design of this junction was taken from the work of Zhang et al. [36]. An enlarged view of the Y-junction is shown in Figure 18a. An s-shaped rectangular waveguide of 0.5 μm, with a bending radius of 90 μm, connects the ends of the Y-junction to the start of the PhCWs. The last 20 μm before the PhCW, the waveguide tapers to fit the width of the PhCWs missing line. The connection between the rectangular waveguide and the PhCW is shown in Figure 18b.

The second type has a rectangular waveguide for the incoupling with the same dimensions as the type 1. After the light is transmitted through an achiral PhCW, it passes through a second rectangular waveguide (dimensions: 220 nm$\times$500 nm), which is connected to a chiral PhCW. The distance between the two PhCWs is 40 μm.

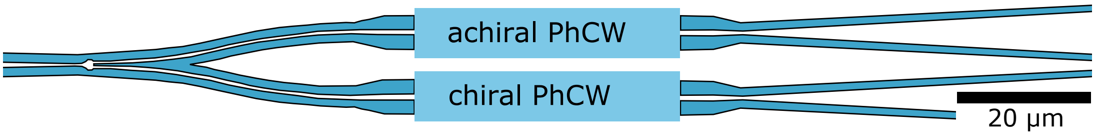

(a) Type 1

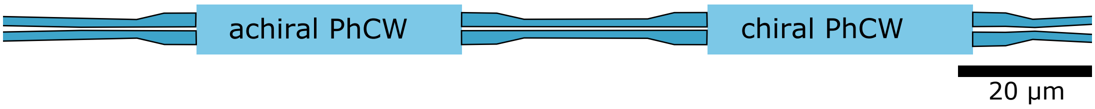

(b) Type 2

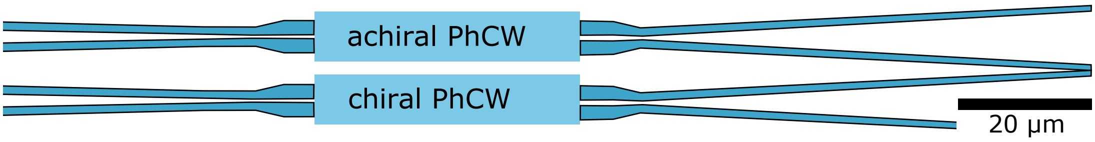

(c) Type 3

Figure 17: Proposed types of incoupling waveguides. The blue area indicates where the silicon would be etched away. The light blue areas are the chiral and achiral PhCWs.

The third type consists of two parallel rectangular waveguides of 3 μm wide and 220 nm high, which each taper to connect to a PhCW, an achiral and a chiral one. The two waveguides are 10 μm apart. This type does not rely on successful fabrication of a Y-junction as type 1 does, or on a high transmission of the light, as type 2 does. However, when the light has been coupled into the achiral PhCW in order to calibrate the setup, the sample must be moved by 10 μm, with the risk of misaligning the sample for the end fire coupling.

For every type, at the end of the last PhCW, a rectangular waveguide guides the light away from the structure over 20 μm, after which it flares out to a width of 10 μm over a distance of 70 μm. In this way, light is dumped into the bulk of the silicon, in order to minimize back-scattering of the light which could add noise to measurements.

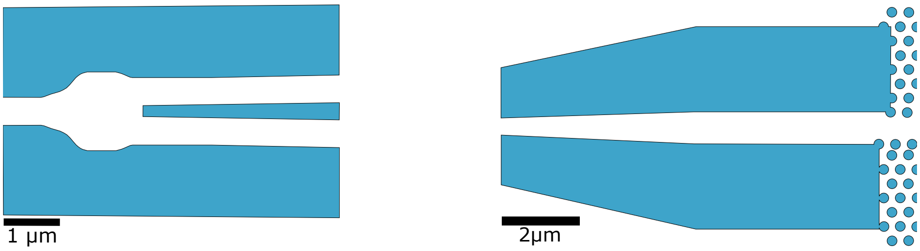

(a) (b)

Figure 18: Details of elements used in the incoupling waveguides. The blue area indicates where the silicon would be etched away. (a) Y-splitter used to divide the incoupling wave in two, as used in type 1. (b) Waveguide that connects a rectangular waveguide to a chiral PhCW.

5 Conclusions

In this work, we have presented a first design for a chiral photonic crystal waveguide, based on numerical simulations, that could be used for on-chip optical rotation measurements. This chiral PhCW requires an optimized optical chirality of its near fields to maximize the chiral interactions with molecules. In order to achieve nonzero optical chirality in the near fields of a PhCW, every symmetry in the system needed to be broken. This was achieved by adding a glass substrate below the silicon slab, and by shifting the two rows of air holes adjacent to the waveguide.

In the well known achiral PhCW, the dispersion of the defect mode is concave and monotonic. As the air holes are shifted to the position of the chiral PhCW, the dispersion becomes non-monotonic. In addition to this, two higher-order modes are pulled down out of the bulk of modes above the waveguide into the band gap. When the holes of the achiral PhCW are shifted in small steps to the positions of the chiral PhCW, the calculated intensity profiles of the fields undergo erratic changes.

We found that the optical chirality of a system is anti-symmetric under mirror reflection. On every mirror plane of an achiral PhCW, the optical chirality was found to be zero. The C-points of these PhCWs were all located on these symmetry planes. Although the light at a C-point is circularly polarized, the optical chirality there is zero. We showed that circular polarization of light does not always correspond to chiral light when at the nanoscale.

The achiral PhCW was found to have superchiral hotspots, one of each handedness next to every air hole along the waveguide. At 20 nm above the silicon, they had a value of $g_{\mathrm{EM}} = \pm 10$. At the air-silicon interface, these same hotspots had a value of ± 24. The chiral PhCW also exhibited strong superchiral hotspots at 20 nm above the surface, with maximum values of $g_{\mathrm{EM}} = -24$ and $+19$. At 200 nm above the surface, the highest value of the local optical chirality in free space was found, with a value of $g_{\mathrm{EM}} = 62$, which is 62 times the value for CPL.

The total optical chirality, which was found by integrating the optical chirality in the air above the chiral PhCW and in the air holes, and normalizing by the electric energy density integrated over the same volume, was found to be 0.16. Thus, it is possible to create a photonic crystal waveguide with chiral near fields. This nanostructure is possibly the first step towards sensitive, on-chip measurements or the optical rotation of chiral molecules.

References

[1] Donald Voet, Judith G. Voet, and Charlotte W. Pratt. *Fundamentals of Biochemistry, Fifth Edition.* Wiley & Sons Ltd, 5 edition, 2016.

[2] PubChem Compound Database. National Center for Biotechnology Information. https://pubchem.ncbi.nlm.nih.gov/compound/36604. CID=36604.

[3] PubChem Compound Database. National Center for Biotechnology Information. https://pubchem.ncbi.nlm.nih.gov/compound/10836. CID=10836.

[4] Laurence Barron. *Molecular Light Scattering and Optical Activity.* Cambridge University Press, 2 edition, 2004.

[5] H A Kramers. *La diffusion de la lumière par les atomes.* 1927.

[6] V Lucarini, J.J. Saarinen, K.-E. Peiponen, and E.M. Vartiainen. *Kramers-Kronig Relations in Optical Materials Research.* Springer, 2005.

[7] John David Jackson. *Classical Electrodynamics.* John Wiley and Sons, 3 edition, 1998.

[8] N. Berova, K. Nakanishi, and R. Woody. *Circular Dichroism: Principles and Applications.* Wiley, 2000.

[9] John Frederick Nye. *Natural focusing and fine structure of light: caustics and wave dislocations.* CRC Press, 1999.

[10] M. Burresi, R. J P Engelen, a. Opheij, D. Van Oosten, D. Mori, T. Baba, and L. Kuipers. Observation of polarization singularities at the nanoscale. *Physical Review Letters*, 102(3):1–4, 2009.

[11] Yiqiao Tang and Adam E Cohen. Enhanced Enantioselectivity in Excitation of Chiral Molecules by Superchiral Light. *Science*, 332(6027), 2011.

[12] Daniel M Lipkin. Existence of a New Conservation Law in Electromagnetic Theory. *Journal of Mathematical Physics*, 5, 1964.

[13] Yiqiao Tang and Adam E Cohen. Optical Chirality and Its Interaction with Matter. *Physical Review Letters*, 163901(April):1–4, 2010.

[14] Yiqiao Tang, Li Sun, and Adam E Cohen. Chiroptical Hot Spots in Twisted Nanowire Plasmonic Oscillators. *Applied Physics Letters*, 102(4), 2013.

[15] Y Liu, W Zhao, Y Ji, R Wang, X Wu, and X D Zhang. Strong superchiral field in hot spots and its interaction with chiral molecules. *Europhysics Letters*, 110, 2015.

[16] Carmelo Rosales-guzmán, Karen Volke-sepulveda, and Juan P Torres. Light with enhanced optical chirality. *Optics Letters*, 37(17):3486–3488, 2012.

[17] Euan Hendry, T Carpy, J Johnston, M Popland, R V Mikhaylovskiy, A J Lapthorn, S M Kelly, L D Barron, N Gadegaard, and M Kadodwala. Ultrasensitive detection and characterization of biomolecules using superchiral fields. *Nature Nanotechnology*, 5(11):783–787, 2010.

[18] Nan Yang, Yiqiao Tang, and Adam E Cohen. Spectroscopy in sculpted fields. *NanoToday*, 4(3), 2009.

[19] Joseph S Choi and Minhaeng Cho. Limitations of a superchiral field. *Physical Review A*, 86(6):063834, 2012.

[20] Nina Meinzer, Euan Hendry, and William L Barnes. Probing the chiral nature of electromagnetic fields surrounding plasmonic nanostructures. *Physical Review B*, 88(4), 2013.

[21] Immo Söllner, Sahand Mahmoodian, Leonardo Midolo, Alisa Javadi, Gabija Kir, Tommaso Pregnolato, Haitham El-ella, Eun Hye Lee, Jin Dong Song, Søren Stobbe, and Peter Lodahl. Deterministic photon – emitter coupling in chiral photonic circuits. *Nature Nanotechnology*, 10(September), 2015.

[22] A Femius Koenderink and Albert Polman. Nanophotonics: Shrinking light-based technology. *Science*, 348(6234), 2015, and references therein.

[23] John Joannopoulos, Steven Johnson, Joshua Winn, and Robert Meade. *Photonic Crystals: molding the flow of light*. Princeton University Press, 2 edition, 2008.

[24] N. Rotenberg, B. Le Feber, T.D. Visser, and L. Kuipers. Tracking nanoscale electric and magnetic singularities through three-dimensional space. *Optica*, 2(6):540–546, 2015.

[25] B Feber, N Rotenberg, D M Beggs, and L Kuipers. Simultaneous measurement of nanoscale electric and magnetic optical fields. *Nature Photonics*, 8(January):1–4, 2014.

[26] M Notomi, K Yamada, A Shinya, J Takahashi, C Takahashi, and I Yokohama. Extremely Large Group-Velocity Dispersion of Line-Defect Waveguides in Photonic Crystal Slabs. *Physical Review Letters*, 87(25), 2001.

[27] Igor A. Sukhoivanov and Igor V. Guryev. *Photonic Crystals*. Springer Berlin Heidelberg, 2009.

[28] T F Krauss. Slow light in photonic crystal waveguides. *Journal of Physics D: Applied Physics*, 40(9):2666–2670, 2007.

[29] Marin Soljačić, Steven G. Johnson, Shanhui Fan, Mihai Ibanescu, Erich Ippen, and J. D. Joannopoulos. Photonic-crystal slow-light enhancement of nonlinear phase sensitivity. *J. Opt. Soc. Am. B*, 19(9):2052–2059, Sep 2002.

[30] Juntao Li, Liam O'Faolain, Sebastian A. Schulz, and Thomas F. Krauss. Low loss propagation in slow light photonic crystal waveguides at group indices up to 60. *Photonics and Nanostructures - Fundamentals and Applications*, 10(4):589 – 593, 2012. TaCoNa-Photonics 2011.

[31] Steven G. Johnson and J. D. Joannopoulos. Block-iterative frequency-domain methods for maxwell's equations in a planewave basis. *Opt. Express*, 8(3):173–190, 2001.

[32] N. Rotenberg and L. Kuipers. Mapping nanoscale light fields. *Nature Photonics*, 8(12):919–926, 2014.

[33] Toshihiko Baba. Slow light in photonic crystals. *Nature photonics*, 2(8):465–473, 2008.

[34] Juntao Li, Thomas P White, Liam O Faolain, Alvaro Gomez-iglesias, and Thomas F Krauss. Systematic design of flat band slow light in photonic crystal waveguides. *Opt. Express*, 16(9):2621–2626, 2008.

[35] Christelle Monat, Bill Corcoran, Majid Ebnali-heidari, Christian Grillet, Benjamin J Eggleton, Thomas P White, Liam O Faolain, and Thomas F Krauss. Slow light enhancement of nonlinear effects in silicon engineered photonic crystal waveguides. *Opt. Express*, 17(4):2944–2953, 2009.

[36] Yi Zhang, Shuyu Yang, Andy Eu-jin Lim, Guo-qiang Lo, Christophe Galland, Tom Baehr-jones, and Michael Hochberg. A compact and low loss Y-junction for submicron silicon waveguide. *Opics Express*, 21(1):1310–1316, 2013.

A Computational cells for simulating a PhCW

A top-down view of the computational cells of the achiral and chiral PhCW is shown in Figure 19. Both slabs consist of 220 nm thick silicon, with bulk SiO_2 filling the half-space beneath them, and vacuum above them and inside the holes of the PhCW. The array of air holes is triangular, and has a lattice constant a of 420 nm. The air holes themselves have a radius of 120 nm. The computational cell contains 22 rows of holes in the y-direction, and a single period in the x-direction. The height of the cell is four times the slab thickness, so the resulting cell is (a, $11\sqrt{3}a$, 880 nm). For the chiral PhCW, the a_1 row was moved in the x and y direction by (0.29, 0.20)a, respectively. The b_1 row, was shifted only in the x-direction by $+0.60a$.

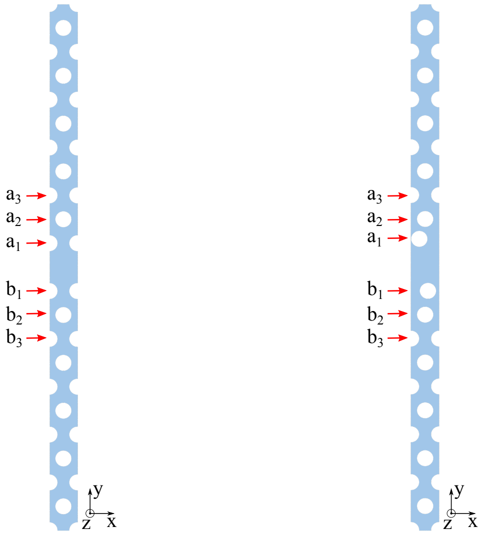

(a) (b)

Figure 19: The computational cells for the (a) achiral and (b) chiral PhCWs. Both slabs consist of 220 nm thick silicon, with bulk SiO_2 filling the half-space beneath them, and vacuum above them and inside the holes in the slab. The array of air holes is triangular, and has a lattice constant a of 420 nm. The air holes themselves have a radius of 120 nm. The computational cell contains 22 rows of holes in the y-direction, and a single period in the x-direction. The height of the cell is four times the slab thickness, so the resulting cell is (a, $11\sqrt{3}a$, 880 nm). For the chiral PhCW, the a_1 row was moved in the x and y direction by (0.29, 0.20)a, respectively. The b_1 row, was shifted only in the x-direction by $+0.60a$.

B Optimization of optical chirality

In order to find an optimal value of the total optical chirality g_{tot} from Eqn. 11, a parameter sweep was done for different positions of the two rows of air holes of the PhCW on either side of the waveguide. This encompassed a sweep of a 4D parameter space. The results of this sweep are shown in Figure 20. The outer axes indicate the different positions of the b_1 row of holes. For every different combination of x and y positions of this row of holes, a 2D sweep of different x and y shifts of the a_1 row of holes was done. For each of these combinations of parameters, g_{tot} was calculated. The result of the sweep shows the highest value of g_{tot} around an (x,y) shift of the a_1 holes of (0.33, 0.14)a and (-0.40, 0.00)a for the b_1 holes in the parameter space explored here, where a is the lattice constant of the hole array. A random walk in parameter space of the a_1 holes yielded a value that was somewhat higher than the one found in the 4D sweep, at $(\Delta a_{1,x}, \Delta a_{1,y})$=(0.29, 0.20)$a$, and $(\Delta b_{1,x}, \Delta b_{1,y})$=(-0.40,0)$a$, with a total optical chirality $g_{\text{tot}} = 0.16$.

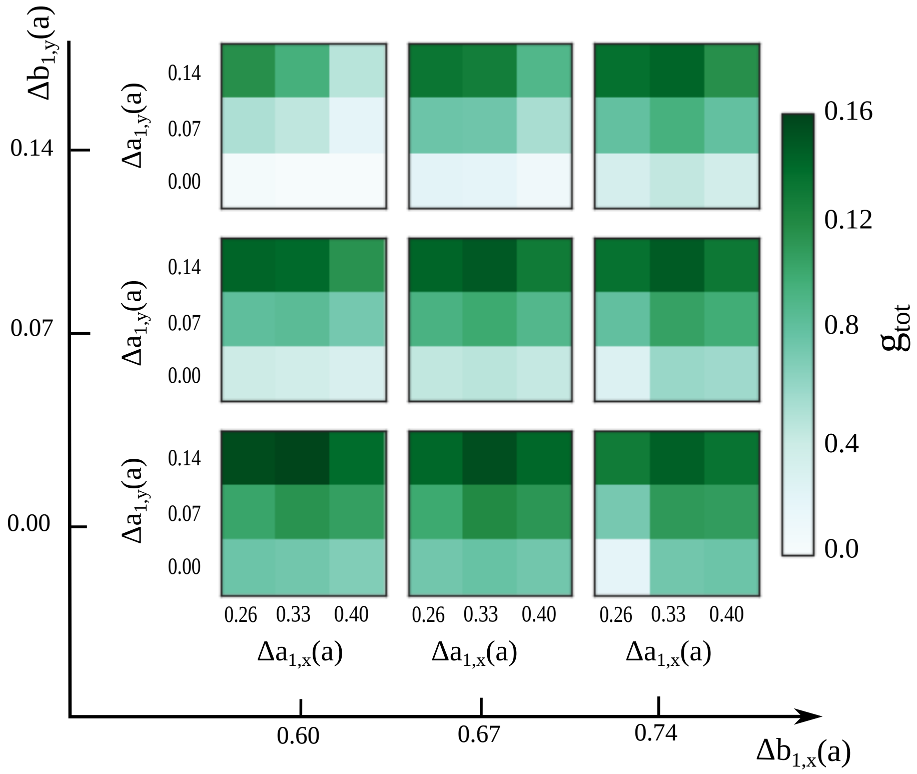

Figure 20: 4D parameter sweep of the position of the first two rows of air holes. The colour scale shows the total optical chirality g_{tot} of the PhCW. The outer axes show the relative shift of the b_1 row of holes in x and y, the inner axes show different positions for the a_1 row.

C Sample fabrication

The achiral and chiral PhCWs were fabricated on a Soitec silicon on insulator (SOI) wafer piece with 220 nm silicon on 1 μm of SiO_2, layered on bulk silicon. The process of fabricating the structures is shown schematically in Figure 21.

The Soitec wafer was sawed to approximately 12×12 mm with a dicing saw. After that, the sample was cleaned with acetone and a small scratch was made on the sample. This scratch will later be used to cleave the sample. To remove any organic material, the sample was treated with base piranha (5:1:1 mixture of H_2O, NH_4OH 30% and H_2O_2 30%) and exposed to an oxygen plasma.

After cleaning, the sample was primed with 1,1,1,3,3,3-Hexamethyldisilazane (HMDS), which was spin coated (Fig. 21a). Then, undiluted Chemically Semi-Amplified Resist (CSAR 62 AllResist CSAR AR-P 6200.09) was spin coated (Fig. 21b). After spin coating, the substrate was cleaved with an edge cleave-tool. This cleaved edge will form a straight end facet for end fire coupling.

The areas of the silicon that needed to be etched away were illuminated with a electron beam (Fig. 21c), which wrote the desired pattern into the resist. The incoupling waveguides were written up to the cleaved edge. After exposure to the electron beam, the resist was developed in pentyl acetate. The development of the resist was stopped in a mix of 4-methyl-2-pentanone and 2-propanol (9:1). Finally, the sample was rinsed in 2-propanol and dried. During this development step, the illuminated resist is removed (Fig. 21d).

In order to remove the oxide layer that forms naturally on the silicon wafer, the sample was etched with a Cl_2 plasma. This is necessary as the plasma used for the next etching step do not etch SiO_2 well. For the etching step, the two cleaved halves of the wafer were laid down with the broken sides adjoining, to reduce effects of the cleaved edge. Then the wafer was etched with HBr and O_2 plasma (Fig. 21e). In this step, the silicon under the removed resist is etched away. The remaining resist is removed by submerging the sample base piranha, and cleaned by rinsing it with water (Fig. 21f).

This fabrication technique was successful. Several scanning electron microscope (SEM) images of the fabricated sample are shown in Figure 22.

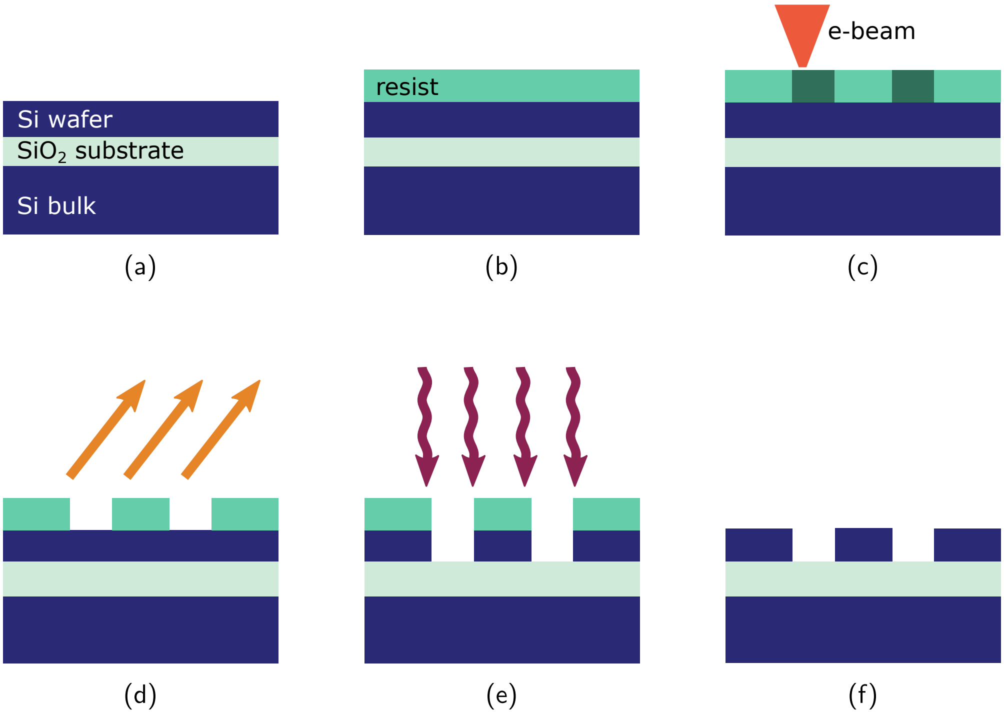

Figure 21: Schematic illustration of the fabrication process (not to scale). (a) Start with a cleaned and primed 220 nm wafer of Si on 1 μm of SiO_2, on a 1 mm Si substrate. (b) Resist was spin coated on. (c) The structures were written into the resist using a focused electron beam (e-beam). (d) The illuminated resist was developed in pentyl acetate. (e) The oxide layer on the silicon was removed with Cl_2 plasma, and the Si under the removed resist was etched with HBr O_2 plasma. (f) The remaining resist was removed with base piranha.

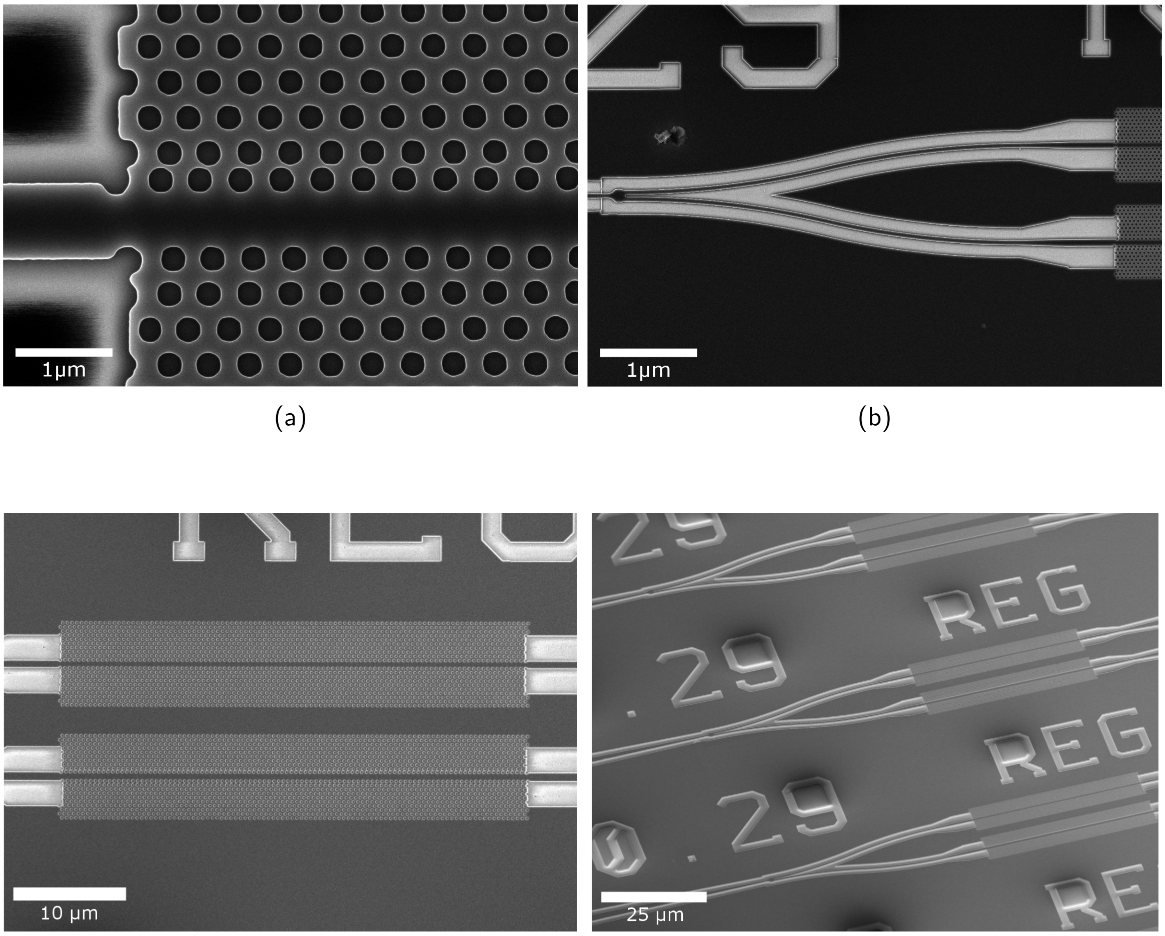

(a) (b)

(c) (d)

Figure 22: SEM images of the fabricated sample. (a) The connection between the rectangular waveguide and the chiral PhCW. (b) The Y-junction of the type 1 PhCW. (c) The achiral and chiral PhCWs above each other, where the achiral PhCW is above the chiral PhCW. (d) The array of type 1 waveguides on the sample.

Acknowlegdements

Many people have contributed to the production of this thesis, and I am grateful to every one of them. Kobus, your boundless enthusiasm for my project and vast knowledge of the workings of light at the nanoscale has made our weekly meetings a pleasure, which I always left with new energy and inspiration. Dolfine, as my direct supervisor and office mate, you helped me with my long-term planning, and were always prepared to help me work out the knots in my brain into organized narratives. I had fun in the lab with you, even if we haven't been able to make everything work yet, and none of it is in my thesis. Filippo, thank you for helping me lay down the mathematical foundations on which I built my thesis. Without your help, many more of my results would have remained unexplained. All of the NanoOptics group, I had a wonderful year working with you, in a friendly and welcoming atmosphere in the group. Whenever I would go to someone for advice, I would receive the answer: "Of course I'll help you! How about right now?" You are great to work with, and you made me feel at home from day one. To Dimitry, Hans and Andries, thank you for the time you took with me to figure out how to best fabricate my sample. Special thanks to Dimitry for putting in many hours to discover the right method of fabricating my sample. I hope that in the future, we will be able to do measurements on it. Last but not least, thank you Gordian, for being at my side, for listening to my troubles and my triumphs, for reminding me to look after myself, and always helping me put my worries into perspective. Thank you all for helping me with my thesis. It's been a great year.